Gas Neutralizer Flowfield Modeling and Experiments

R. A. Martin* and M. C. Cline†
Los Alamos National Laboratory, Los Alamos, New Mexico
and
E. P. Muntz‡ and T. Farnham§
University of Southern California, Los Angeles, California

A gas neutralizer internal flowfield is computed using the Navier-Stokes code VNAP2 to assess the code's value as a gas neutralizer modeling tool and to provide design calculations. The steady-state, viscous, continuum field is produced by injecting argon gas radially into a cylindrical tube at the midplane. Inflow conditions are selected in accordance with design requirements to optimize the conversion of ions to neutral particles. Results from the calculations include the velocity field, contours of Mach number and density, axial and radial profiles of density, and axial profiles of the argon target thickness parameter. In addition, measurements inside a ⅓-scale gas neutralizer model are performed to benchmark the code. Density field measurements are obtained using the electron-beam fluorescence technique, and limited pressure measurements are obtained from wall static pressure taps and a free molecular probe in the tube end. The two-dimensional code predictions are in reasonably good agreement with the three-dimensional experimental results, showing that VNAP2 is useful for future qualitative gas neutralizer design calculations.

Nomenclature

a = speed of sound
A = area of tube cross section
b = background
D = tube diameter
H = hydrogen ion
k = coefficient of thermal conductivity
Kn = Knudsen number
L = tube length
$\dot{m}$ = mass flow rate
M = Mach number
n = direction normal to wall
N = ionic fraction
p = pressure
r = coordinate direction along tube radius
Re = Reynolds number
T = temperature
u = z component of velocity
v = r component of velocity
W = slot width
z = coordinate direction along tube axis
γ = specific heat ratio
λ = second coefficient of viscosity
μ = first coefficient of viscosity
ρ = density
σ = collision cross section
χ = target thickness

Subscripts

e = tube ends
i = injection slot or index
m = model
max = maximum
p = prototype
w = wall
0 = stagnation or reservoir
$(\ )_*$ = sonic

Introduction

THE Strategic Defense Initiative includes the national Neutral Particle Beam (NPB) program. A long-term objective of the program is to operate an NPB accelerator system in space. The beam generated by this device could be used in discrimination experiments to differentiate between objects of high and low mass. At Los Alamos National Laboratory, a ground-based engineering prototype facility called the ground test accelerator (GTA) is being designed and constructed to demonstrate the performance of an integrated and automated NPB system.[1] This facility will provide a demonstration test bed and technology transfer of experience and hardware between Los Alamos National Laboratory, and industrial contractors.

One subsystem of the GTA, shown schematically in Fig. 1, is the neutralizer. The neutralizer is the last physical device in the GTA through which the negative hydrogen ion beam passes after having been accelerated and shaped by time-varying magnetic fields produced in earlier stages. Its function is to convert the high-energy ionic beam developed in the accelerator to a beam of neutral particles. Neutral particles are required because such particles are unaffected by the Earth's magnetic fields or local magnetic fields and, therefore, will propagate in a straight line to the target.

A number of neutralizer concepts have been considered at Los Alamos National Laboratory and elsewhere, including gas cells, foils or films, gas jets, and photodetachment (using lasers).[2,3] One attractive concept is the ring nozzle, studied in detail by Brook et al.[4] In each case, efficient production of neutrals and minimal contribution to the beam divergence are desirable; other design factors such as complexity, size, mass, and power requirements are also important. For GTA, the primary concepts are foils and gas cells.

Gas cell neutralization is a relatively mature technology for which most of the key issues are understood and data are

---

Presented as Paper 87-1517 at the AIAA 22nd Thermophysics Conference, Honolulu, HI, June 8-10, 1987; received June 9, 1987; revision received April 1, 1988.

*Group MEE-13 Staff Member. Member AIAA.

†Group T-3 Staff Member. Member AIAA.

‡Cochairman and Professor, Department of Aerospace Engineering. Fellow AIAA.

§Research Assistant, Department of Aerospace Engineering. Student Member.

available or can be extrapolated. A challenge for gas cell technology lies in the gasdynamic and cryogenic design of large-bore systems. However, work is needed to optimize gas cell designs for NPB applications.

One gas cell design for the GTA is the axial flow cylindrical tube shown schematically in Fig. 2. Here the target gas is injected radially through a circumferential slot (or through a row of holes) in the tube wall to form a gas cloud inside the tube. The ion particle beam enters the tube on the left and passes coaxially through the tube encountering atoms of the argon target along the way. Conversion (or electron stripping) of negative hydrogen ions occurs via the coulomb collision mechanism. The ends of the tube exhaust into chambers maintained at vacuum conditions by cryopumping equipment. External vacuum conditions are required to prevent gas leakage, which can cause prestripping of hydrogen ions in the upstream beam-steering and telescope sections of the GTA, and to prevent interference with beam-sensing experiments performed downstream of the neutralizer (see Fig. 1). Thus, design calculations are needed to optimize the target thickness distribution (density variations) for a given beam energy, geometry, and gas, and to produce minimal gas leakage (minimal mass flow rate).

In the work reported here, Navier-Stokes code VNAP2 is modified and used to compute the GTA gas cell neutralizer flowfield to assess the code's value as a modeling tool, to provide design calculations, and to obtain a better understanding of the complex flow. VNAP2 can calculate turbulent (as well as laminar and inviscid), steady, and unsteady flow. VNAP2 uses the second-order, MacCormack finite-difference scheme to solve the two-dimensional, time-dependent, flow equations for perfect gases. A variable mesh spacing can be used. The code is quite general and was originally optimized for application to a wide variety of both internal and external aerodynamic flowfields. However, the present application poses a complex flowfield not considered previously. This application required modifications to the method by which the boundary conditions are computed. It is also necessary to provide for mass injection through an opening in the flow boundaries (walls) to simulate radial gas injection into the neutralizer. VNAP2 is available from the second author on request.

Results of the calculations are compared to experimental measurements inside a ⅓-scale model gas cell neutralizer to benchmark the code. The VNAP2 calculations were performed before the experiments were run. Density field measurements are obtained using the electron-beam fluorescence technique, and limited pressure measurements are obtained from wall static pressure taps and a free molecular probe at the University of Southern California (USC).

Neutralizer Description

Gas cell neutralizer design is determined principally by beam energy and size. An early specification for the GTA beam is 50-MeV energy and 25 cm in diameter. Engineering considerations lead to one solution, shown graphically in Fig. 2. When a high-energy H^- beam passes through a "thin" target, charge changing occurs because of "collisions" between the beam and target. The target may be atoms, molecules, ions, free electrons, or photons. The incident H^- beam is converted to the three charged beams H^-, H^0, and H^+ with fractions N^-, N^0, and N^+, respectively. The growth and decay of these fractions depend on the target thickness

$$\chi = \int \rho \mathrm{d}z \tag{1}$$

where χ is the target thickness (also known as areal density, column depth, line density, or optical thickness) with units of mass or particles per unit area, ρ the mass or number density, and z the path length for which charge changing is appreciable. Equation (1) can be interpreted as the area under a ρ vs z curve. Reference 5 presents an approximate mathematical model of the physical process which includes three coupled, first-order, linear ordinary differential equations for the rate of change of N with respect to χ. These rates depend on three measurable conversion cross sections. σ_i, $i = 1,2,3$ and the amount of each species present. Conversion of H is represented by σ_i from minus to zero, minus to plus, and zero to plus, respectively. They are a function of beam energy and have units of area per particle. The solution of this linear system leads to $N^0 = N^0(\sigma_i, x)$, and setting $\mathrm{d}N^0/\mathrm{d}\chi = 0$ allows solution of $\chi_{\max} = \chi_{\max}(\sigma_i)$, the optimum target thickness that produces the largest H^0 beam, $N^0 = 0.53$. Using this equation for $\chi_{\max}$ and known values for σ_i for a 50-MeV beam and argon gas gives $\chi_{\max} = 4.73 \times 10^{-5}$ kg/m^2 = 7.13×10^{16} atoms/cm^2 for optimal production of neutrals.[6]

Approximating the flowfield of Fig. 2 with idealized sonic conditions throughout the cell, it can be shown that[6]

$$(\dot{m}_*)_{\max}/A_* = C(\gamma)(\chi/L)a_0 \tag{2}$$

where $(\dot{m}_*)_{\max}$ is the mass flow rate out the ends of the tube, A_* the total sonic area, $C(\gamma)$ a constant that depends only on the ratio of specific heats, L the length of the tube, and a_0 the stagnation sound speed. Equation (2) allows evaluation of the effect of L and the type of gas on leakage. Thus, further engineering compromises to minimize $(\dot{m}_*)_{\max}/A_*$ and the beam divergence (a function of neutralizer length, L) led to the selection of a 30-cm diam (to allow for beam steering and to avoid scraping of the 25-cm beam), 100-cm long ($L/D = 3.33$) GTA prototype neutralizer using argon gas for the target. The GTA design parameters are given in Table 1.

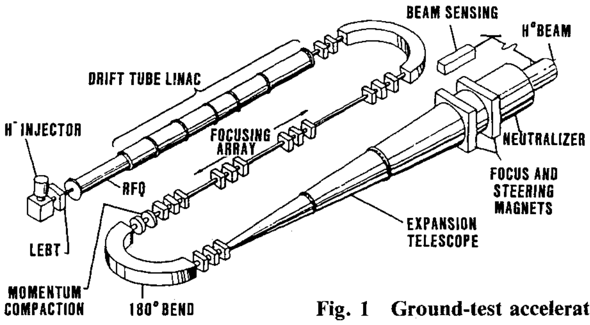

Fig. 1 Ground-test accelerator.

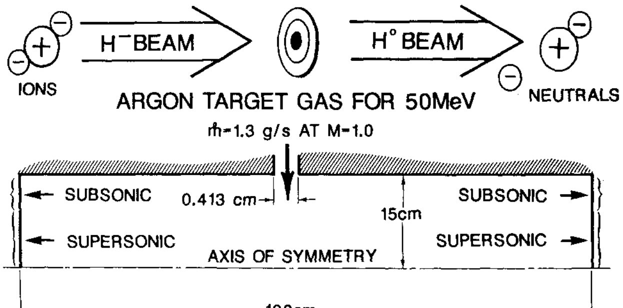

Fig. 2 GTA gas cell neutralizer concept.

Table 1 GTA neutralizer design parameters

Parameter	Value
Beam energy	50 MeV
Beam diameter	25 cm
Tube diameter	30 cm
Tube length, L	100 cm
Gas	Argon
Target thickness, χ	4.73×10^{-5} kg/m^2

For simplicity, the beam energy is assumed to be constant at 50 MeV over its 25-cm diam. For a real beam, the energy will have a Gaussian shape centered about the axis of symmetry. Thus, a Gaussian shape to the radial profile of χ is desirable in a real neutralizer.

Flow Model

Flow Description

In the gas neutralizer flow experiments presented later in this paper, gas was injected through a circumferential ring of discrete holes. To compute the flow in such a situation would require a fully three-dimensional calculation with an extremely fine grid. To avoid this complexity, the discrete holes were modeled as a circumferential slot having the same mass flow as the discrete hole configuration. Because the spacing between holes is large compared to the hole diameter, setting the slot area equal to the sum of the areas of the discrete holes would result in an excessively narrow slot requiring an extremely fine grid. To avoid this problem, slot widths of approximately 0.8 cm and 0.4 cm were chosen arbitrarily. The total pressure was adjusted to provide the desired mass flow. Because the 0.4-cm slot produced the best agreement with experiment, only those results are shown here.

The flow geometry is shown in Fig. 2. Because the tube cross section is circular, the flow is assumed to be axisymmetric. Therefore, the computational boundary includes the entire upper-half plane bounded horizontally by the tube ends and vertically by the axis of symmetry and the tube wall (denoted by the shading). The physical dimensions of the computational plane are 100 × 15 cm as shown. Flow enters through a circumferential slot of width $W_* = 0.4125$ cm at sonic conditions. Because of symmetry, the flow divides inside the tube and exits in equal amounts through the left and right ends. The computational grid corresponding to Fig. 2 is shown in Fig. 3. This grid was used in the VNAP2 computations presented here.

To estimate the mass flow rate of argon required to produce the target thickness χ given in Table 1, idealized, uniform sonic conditions were assumed throughout the tube.[6] This assumption leads to the VNAP2 modeling parameters given in Table 2. Note that the calculations are based on an assumed effective sonic tube diameter of $D_* = 25$ cm to account approximately for viscous effects. Thus, an estimated mass flow rate of $\dot{m}_* = 1.3$ g/s was used to calculate the injection slot stagnation and static conditions summarized in Table 2.

While VNAP2 calculations with different tube lengths, slot widths, boundary conditions, and grid spacings were made, only the long tube, narrow slot, and finest grid case is presented here. The injection parameters are given in Table 2. Also shown is the experimentally measured (and scaled or reduced by a factor of 3) tube end pressure $p_e = 1.04$ Pa used as a boundary condition for VNAP2.

Governing Equations

In low density and, therefore, low Reynolds number flows, viscous effects are important throughout the flowfield. Therefore, such simplifying assumptions as those involved in the viscous boundary-layer/inviscid external flow model are not appropriate. In addition, the neglect of streamwise viscous effects, as in the parabolic and thin-layer Navier-Stokes equation models, is questionable. For these reasons, the full two-dimensional, time-dependent, compressible Navier-Stokes equations for an ideal gas in thermal equilibrium are solved[7] to determine the velocity field (u,v) in axisymmetric geometry (r,z) and to determine the pressure and density fields p and ρ, respectively.

The steady-state flow, when it exists, is the transient solution for large time. The flow is assumed to be laminar. The fluid is argon and is considered to be an ideal gas with a constant ratio of specific heats, $\gamma = 1.67$. The coefficients of viscosity, μ, and thermal conductivity, k, are

$$\mu = 3.164 \times 10^{-7}\, T^{0.75} \text{ (Pa-s)} \tag{3}$$

$$k = 1.4 \times 10^{-4}\, T^{0.85} \text{ (W/m-K)} \tag{4}$$

The second coefficient of viscosity, λ, was set equal to $-2\mu/3$. To stabilize these calculations in the shock-wave region, an explicit artificial viscosity, based on the velocity

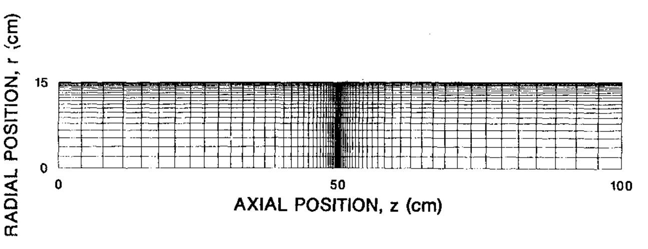

Fig. 3 Computational grid.

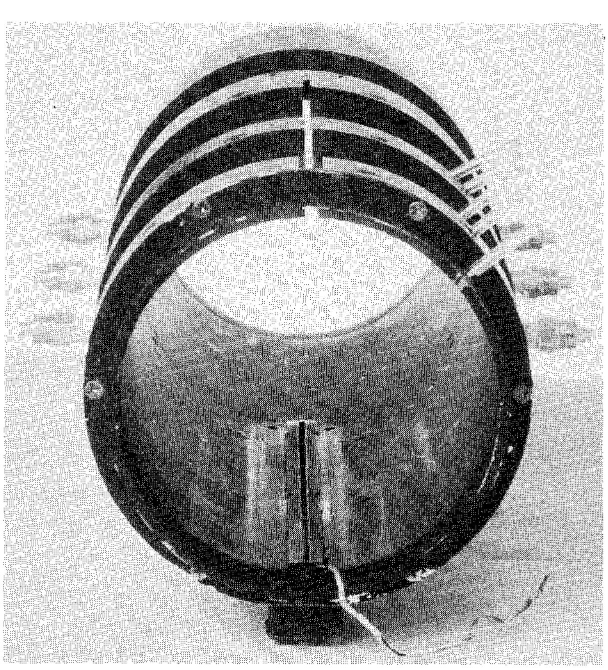

Fig. 4 One-third-scale model neutralizer end view.

Table 2 VNAP2 modeling parameters

Parameter	Value
Tube diameter, D	30 cm
Assumed effective diameter, D_*	25 cm
Tube length, L	100 cm
Density, ρ_*	4.73×10^{-5} kg/m^3
Pressure, P_*	2.215 Pa
Static temperature, T_*	225 K
Stagnation temperature, T_0	300 K
Slot width, W_*	0.4125 cm
Mass flow rate (estimated), $\dot{m}_*$	1.3 g/s
Injection stagnation pressure, p_{0i}	0.119 Pa
Injection stagnation temperatures, T_{0i}	300 K
Injection static pressure, p_{*_i}	57.4 Pa
Injection static temperature, T_{*_i}	225 K
Injection static density, ρ_{*_i}	1.24×10^{-3} kg/m^3
Injection sonic velocity, v_{*_i}	279 m/s
End pressure (measured at USC), p_e	1.04 Pa
Pressure Ratio p_{0i}/p_e	114
Mean free path, MFP	2.3 mm
Knudsen number, Kn_D	0.0076
Reynolds number, Re_D	230

and sound-speed gradients, was added to the molecular values. For additional details see Ref. 7.

Boundary Conditions

From Fig. 2, it is seen that the flow enters the tube from a circumferential slot and exits via the left and right ends. The flow entering the tube is sonic and, therefore, all flow variables are specified. However, the flow at the tube ends will be a mixture of subsonic and supersonic flow and may contain inflow for certain exit pressures. Therefore, the following boundary conditions were imposed:

1) Subsonic outflow: Specify p, calculate u, v, and ρ.
2) Supersonic outflow: calculate all variables.
3) Subsonic inflow: specify p, v, and ρ; calculate u.

The above boundary conditions worked well for cases with fairly high exit pressure. However, for low exit pressures, very large pressure gradients in the r direction were set up at adjacent grid points, where the flow was subsonic at one point and the supersonic at the other. To correct this tendency, the pressure was specified for outflow, regardless of the Mach number. The value of pressure chosen was the maximum of either the specified exit pressure (measured in the experiments) or 50% of the pressure at the next upstream grid point. (Values of 80 and 90% also were used and produced little difference in the results.) This caused the pressure at the exit to drop until the flow either reached the specified value or it could no longer accommodate a lower value. Any errors that occur as a result of specifying the pressure for supersonic outflow do not propagate upstream in the supersonic flow.

The lower boundary of Fig. 2 or Fig. 3 is the tube centerline, where flow symmetry is enforced. The upper boundary is the tube wall, which is assumed to have no velocity slip and to be adiabatic, i.e., at $r = r_w = 15$ cm: $u = v = 0$, $\partial T/\partial n = 0$, where the subscript w denotes the wall value and n denotes the direction normal to the wall.

Numerical Method

The interior grid points in the VNAP2 code were computed using the unsplit MacCormack scheme.[8] The unspecified variables at the grid points on the wall were calculated using a characteristic scheme, while the variables at the left and right boundary points were extrapolated from the values at interior points. For further details on the VNAP2 code, see Ref. 7.

The computational grid is shown in Fig. 3. The variable mesh grid has dimensions of 66 × 23, for a total of 1518 grid points. The grid was refined in the r direction near the wall to resolve the viscous boundary layer as well as the flow exiting the slot. The grid was also refined in the z direction in the region of the slot opening.

Similitude

Dynamic similarity between a prototype p and model m neutralizer at a given beam energy implies equal target thicknesses,

$$\chi_p = \chi_m = \text{const} \tag{5}$$

for equal charge conversion regardless of scale. This is equivalent to

$$p_p D_p = p_m D_m = \text{const} \tag{6}$$

Using this condition and assuming $T_p = T_m$ and geometric similarity (so that the velocity fields at scaled locations are identical), then[9]

$$\begin{aligned} M_p &= M_m \\ Kn_p &= Kn_m \\ Re_p &= Re_m \end{aligned} \tag{7}$$

and

$$\frac{\dot m_p}{\dot m_m} = \frac{p_m}{p_p} = \frac{\rho_m}{\rho_p} = \frac{D_p}{D_m} = \frac{\text{MFP}_p}{\text{MFP}_m} \tag{8}$$

Thus, a model will operate at a lower mass flow rate, but at a higher pressure and density. Equation (8) was used to design

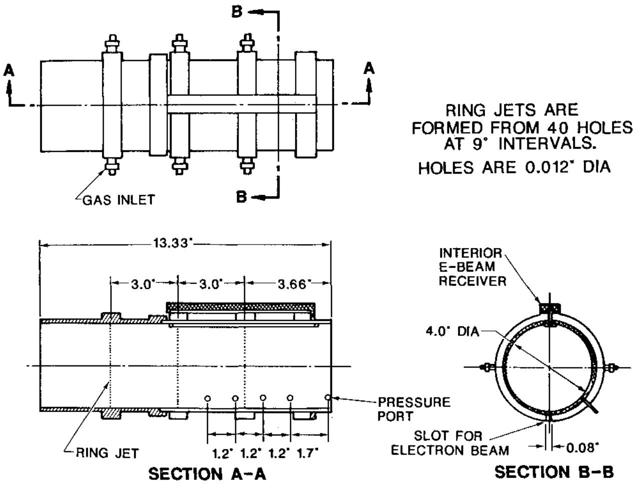

Fig. 5 Model neutralizer dimensions.

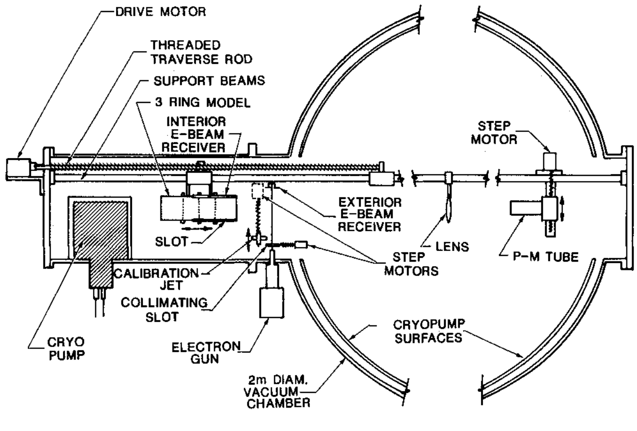

Fig. 6 USC vacuum test facility with model and E-beam.

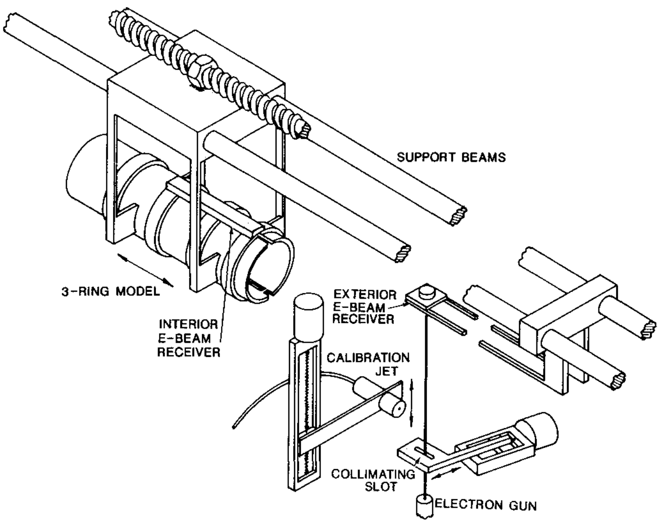

Fig. 7 E-beam calibration and model configuration.

the experiments and to scale up the data for comparison to VNAP2 calculations.

Experiments

Apparatus and Instrumentation

The experiments were conducted using a ⅓-scale model of the neutralizer. A photograph of the model is presented in Fig. 4. Model dimensions and placement in the test facility are shown in Figs. 5 and 6. The model was installed in a 2-m-diam × 2-m-long cylindrical stainless steel vacuum chamber. The facility is pumped by a 61-cm oil diffusion pump and two cryogenic condensation pumps. The main condensation pump has a capacity of about 150 W at 20 K, and a smaller secondary condensation pump has a capacity of about 30 W at 30 K. The large condensation pump is used to supply condensation panels that cover the entire inner cylindrical surface of the facility.

The model neutralizer was mounted on a transversing mechanism as illustrated in Fig. 6. Most of the measurements were obtained using the electron-beam fluorescence technique to measure gas density in the model flowfield.[10] The small condensation pump was used to pump gas in the blind tube, which was used to permit the model to transverse the electron beam as illustrated in Fig. 6 (in which the positions of the main experimental components are indicated). Following the prescription for successful density measurements using the electron-beam fluorescence technique,[10] the electron-beam, shown in Fig. 6, remained stationary and the flowfield was traversed relative to it during the experiments. The flowfield was studied from several diameters ahead of the neutralizer to one-eighth diameter beyond the tube's midplane (z = 50 cm). Different radial positions could be observed by adjusting the photomultiplier tube (EMI 6256S) and the optical filters to be at different radial positions along the image of the electron-beam fluorescence. The photomultiplier tube (PMT) had an entrance aperture 3 mm high × 10 mm wide, so that, effectively, the spatial resolution of the fluorescence measurement was close to 3 mm by the 3-mm beamwidth.

A perspective of the major experimental components is shown in Fig. 7. Notice that the E-beam enters the model through a 5-mm slot and is measured using a linear E-beam receiver in the upper wall of the model. The width of the beam was controlled by the preslot illustrated in Fig. 7. Both the external and internal E-beam receivers had inner and outer sensor areas ("cup and plate"), so that the location of the E-beam could be repeated accurately by adjusting the current ratio between the inner and outer receiver areas.

The E-beam fluorescence generated by the 20-keV beam used in the experiments was linear, with density for the density range of interest as illustrated by the calibration curve shown in Fig. 8. Again, following the technique of Ref. 10, the calibration was done using a free-jet flowfield, which could be translated to any position along the length of the E-beam. The calibration jet setup is shown in Fig. 7. Argon was used in all of the experiments. An optical filter was used to observe only the 460.96-nm line of argon as recommended by Muntz.[10]

A limited number of centerline and wall static pressure measurements were obtained. The wall taps are shown in Figs. 4 and 5. These were measured with an MKS Baratron using a 12-station Scanivalve for obtaining sequential measurements from a number of pressure leads. During the experiments, the argon mass flow was 0.403 g/s (instead of the correct scaled value of 0.43 g/s), which resulted in a vacuum chamber background pressure of around 2×10^{-4} Torr. This entire gasflow was injected through a single ring of 40 holes of 0.3048 mm in diameter, equally spaced around the wall circumference at the midplane of the model.

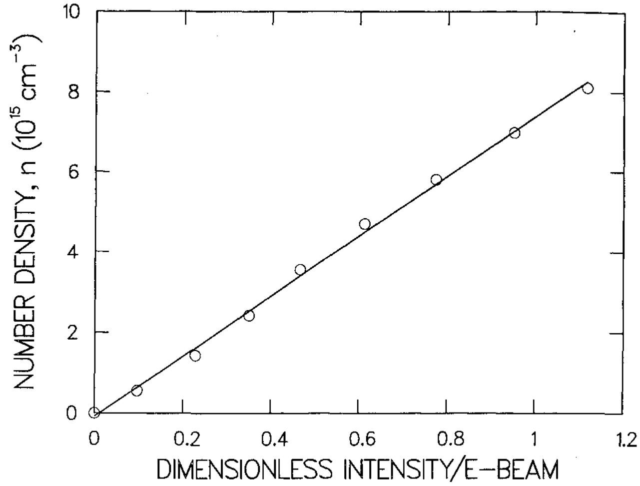

Fig. 8 E-beam system calibration.

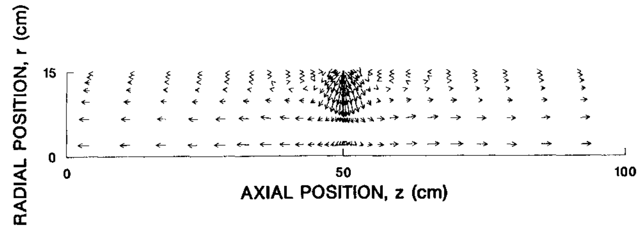

Fig. 9 VNAP2 velocity field.

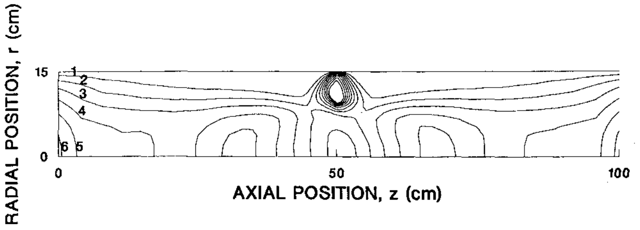

Fig. 10 VNAP2 Mach number contours (1 = 0.33, 2 = 0.67, 3 = 1.00, 4 = 1.33, 5 = 1.67, 6 = 2.00).

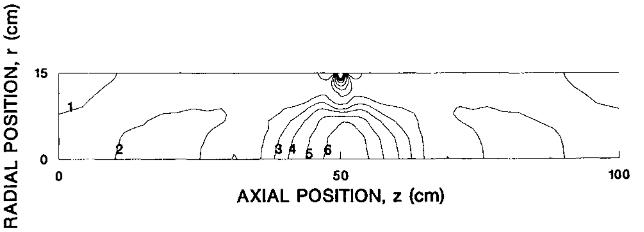

Fig. 11 VNAP density contours (1 = 0.000050, 2 = 0.000065, 3 = 0.000080, 4 = 0.000100, 5 = 0.000130, 6 = 0.000160, all in kg/m^3).

Experimental Procedure

The PMT was turned on and fatigued for several hours prior to an experiment. To obtain data, the PMT was positioned at the desired radial location in the flowfield. (The E-beam passed through the flow centerline perpendicular to it.) The model was retracted so that the E-beam was 1- to 2-model diameters ahead of the model. Gas flow was turned on and the model axial traverse was started. The model axial location was indicated during a traverse by the voltage picked off from a 10-turn potentiometer supplied with a 2.52-V total potential drop. The PMT current was shunted to ground through a 10^4-Ω resistor, and the output was smoothed with a 0.1-s filter. Both signals were digitized using a Hewlett-Packard (HP) 3497A data acquisition unit, and they were stored using an HP 9000-series computer. The electron-beam current was also recorded by the computer during each run. Approximately 100 to 300 points were obtained per run. Calibrations were obtained several times during a series of data runs by retracting the model and traversing the calibration orifice into position. The free-jet flowfield produced by such an orifice is determined entirely by the mass flow rate through the orifice. In particular, the density, as a function of downstream location and mass flow rate, may be derived from the equations given in Ref. 11. Calibrations were always done at a distance of 2.8 cm from the 1-mm-diam orifice. All mass flows were measured for both the flowfield and the calibration using the same Fisher and Porter flow meter.

Data Reduction

As seen in Fig. 8, the calibration curve of argon number density vs E-beam fluorescence intensity per unit E-beam current is quite linear. Number densities are obtained from the experiments by calculating the fluorescence intensity per unit beam current for a particular point in the flowfield and by converting to number density using the slope of the appropriate calibration curve. Measured densities as a function of position are thus readily available from the data by manipulating stored arrays of position, fluorescence intensity, and beam current.

Results

Calculations

The calculated velocity field is shown in Fig. 9. The underexpanded argon gas expands out of the slot at a pressure ratio of $p_{0i}/p_e = 114$, is compressed by a thick shock between approximately $r = 10.5$ cm and 6.6 cm, and forms a stagnation point on the axis of symmetry where the cross-sectional area for radial flow is zero. The no-slip boundary condition is imposed along the tube wall. Other flowfield features include a shear region surrounding the jet with recirculating ring vortices on either side near the wall. Longitudinal pressure gradients are set up from the midplane to the tube ends, which cause the gas to turn toward the tube ends. On the ends, the conditions are mixed subsonic and supersonic outward flow. The flow in the upper- or outer-third radius is a subsonic sheath of boundary layer surrounding an inner supersonic core that diffuses outward to about $M = 2.1$ on the center line at the exit plane.

Figure 10 shows the calculated Mach number contours. It is evident here that steep gradients in the torroidal-shaped jet plume occupy approximately the outer-third radius of the tube near the midplane ($z = 50$ cm). The peak Mach number on the midplane is $M = 4.1$ at $r = 10.5$ cm because of the downward expansion. Along the tube axis, a weak overexpansion to $M = 1.9$ and recompression occur before the flow reaccelerates because of the low exit-plane pressure of $p_e = 1.04$ Pa. Contour 3, the sonic line, curves upward toward to the wall near the ends of the tube but does not intersect the lip. A slight skewing of the contours to the right in Fig. 10 is caused by the unsymmetrical numerical scheme that was rotated to minimize this effect.

Calculated density contours that allow evaluation of radial target thickness variations are presented in Fig. 11. Referring to Fig. 12, it can be seen that the radial variation of density is only about 10% out to the midradius. Further out on the midplane, the thick shock-compression region is evident from $r = 10.5$ to 6.6 cm. The nearly fourfold increase in density in this shock is consistent with the theoretical strong-shock limiting value.

The results of numerically integrating the calculated density field to obtain the target thickness [Eq. (1)] along 23 radial positions are shown in Fig. 13. Computed results are shown for tube lengths of 100 cm ($L/D = 3.33$) and 30 cm ($L/D = 1$) and can be compared to the target thickness for idealized sonic conditions (4.73 μg/cm^2). Evidently, a mass flow rate of $\dot{m}_* = 1.3$ g/s is more than is required at all radii to convert a uniform ion beam of 50 MeV. (A real beam energy profile is Gaussian in shape.) Possible tradeoffs include reducing the mass flow rate or shortening the tube. Note that the contribution of the density field to the target thickness χ, for $z < 35$ cm and $z > 65$ cm (or the outer 70 cm of tube length), is significant and more than doubles χ for the same mass flow rate.

Measurements

The measured density field in the ⅓-scale experimental model is shown in Figs. 14-18. Assuming symmetry of flow about the midplane, the data are reflected through $z = 50$ cm for comparison with the code predictions. In Figs. 14-16, the spherical zone of decreasing density centered at the stagnation point is seen to fall off rather sharply in the axial direction on either side of the midplane, with overexpansion and recompression near the axis. Notice that the estimate of $\rho_* = 0.473 \times 10^{-4}$kg/m^3, given in Table 2, was reasonable for the background density away from the midplane. Measured radial profiles of density are shown in Fig. 12, and radial profiles of target thickness are shown in Fig. 13 for 5 radial positions. These measurements are believed to be accurate in absolute density to within 5%.

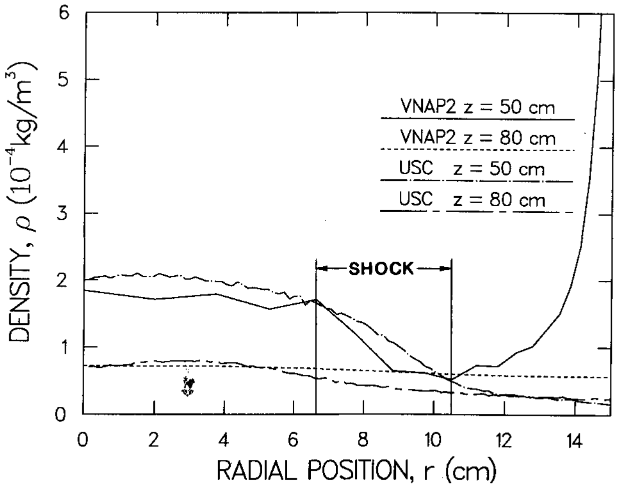

Fig. 12 Comparison of VNAP2 prediction to USC radial density data.

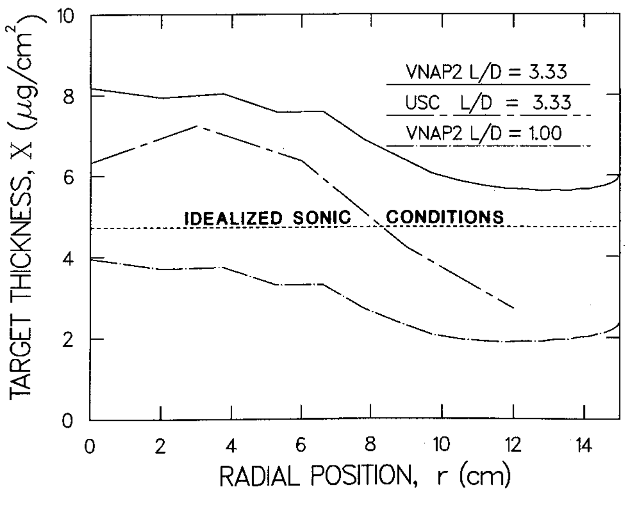

Fig. 13 Comparison of VNAP2 prediction to USC radial target thickness.

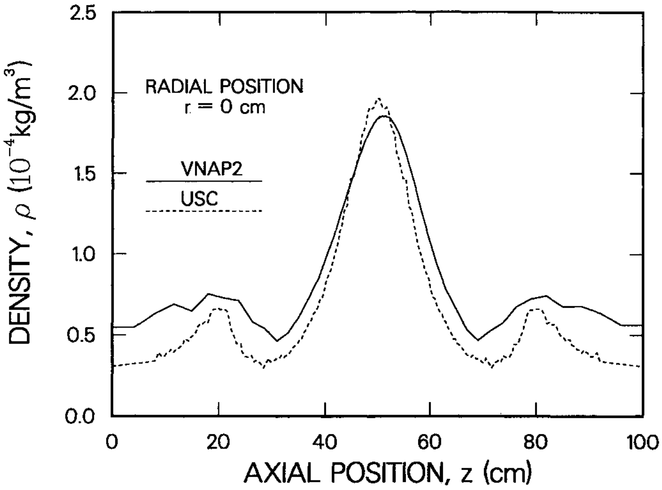

Fig. 14 Comparison of VNAP2 prediction to USC axial density data for $r = 0$ cm.

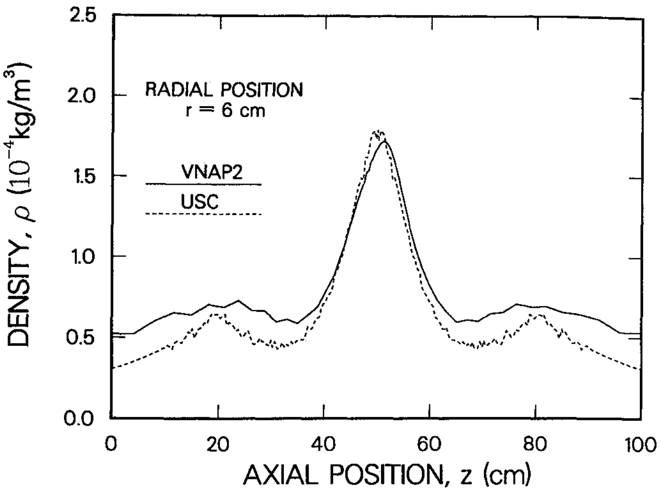

Fig. 16 Comparison of VNAP2 prediction to USC axial density data for $r = 6$ cm.

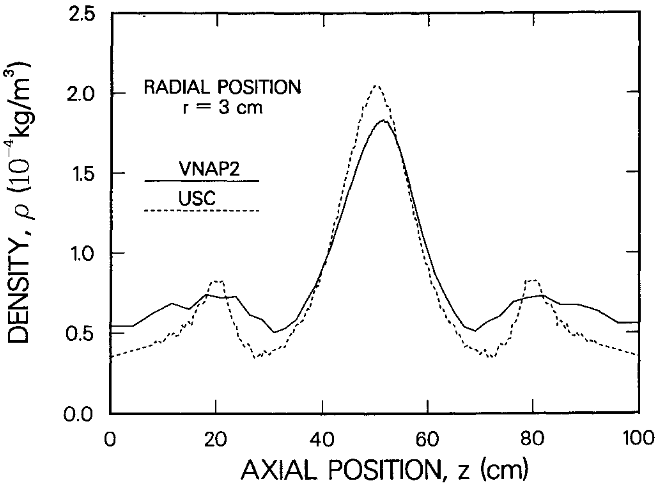

Fig. 15 Comparison of VNAP2 prediction to USC axial density data for $r = 3$ cm.

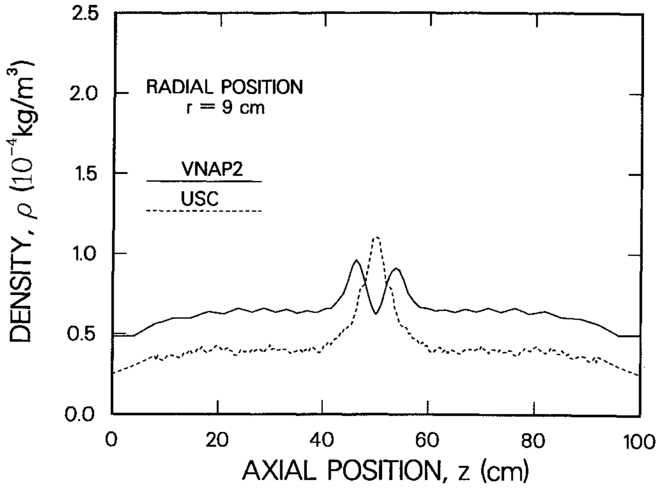

Fig. 17 Comparison of VNAP2 prediction to USC axial density data for $r = 9$ cm.

Comparisons

To assess the value of VNAP2 as a gas neutralizer modeling tool, code predictions are compared to experimental data in Figs. 12–18. Axial profiles of density for 5 radial positions are compared in Figs. 14–18. A cubic spline interpolation routine was used to fit the VNAP2 data along 66 radials and return 5 interpolated points at $r = 0$, 3, 6, 9, and 12 cm for comparison. The agreement is reasonably good over the entire tube for $r = 0$, 3, and 6 cm (Figs. 14–16). The peak densities are predicted to within about 10%, and the densities elsewhere agree to within a factor of 2. For radial positions $r = 9$ and 12 cm (Figs. 17 and 18), mostly in the subsonic boundary layer. VNAP2 predictions are higher by about a factor of 2.

Returning to Fig. 12, it is seen that the predicted radial distribution of density agrees reasonably well with the experimental data between $r = 0$ and 6.6 cm (see also Figs. 14–16), as does the shock location. For values of r in excess of 10.5 cm in the midplane, the VNAP2 density increases steeply to the continuous slot sonic injection condition of $\rho_{*_i} = 12.4 \times 10^{-4}$ kg/m^3. The experimental data show no such increase because of the E-beam orientation between two of the discrete 40 holes.

A comparison of radial target thickness is made in Fig. 13. Because of lower measured densities in the boundary layer (Figs. 12, 17, and 18) and on either side of the jet (Figs. 14–16), particularly near the tube ends, VNAP2 predicts from about 15% to two times higher target thickness. The large discrepancy in density and, therefore, in target thickness near the wall may be partially explained in Table 3. Table 3 shows that the measured value of pressure on the wall is 46% lower than the calculated value (point 1). This is because the calculation boundary condition was assumed to be a uniform pressure equal in value to the measured pressure on the centerline (point 6).

The exact cause of the differences observed in Table 3 and Figs. 12–18 is not clear. The main contribution to the differences may be that the calculation does not property treat the expansion caused by the sudden area change at the end of the experimental model tube and exhaust into a background pressure of about $p_b = 2 \times 10^{-4}$ Torr $= 2.67 \times 10^{-2}$ Pa. Thus, the experimental model serves as a large-bore free-jet source to the vacuum chamber with a pressure ratio of about $p_e/p_b = (1.04)/(2.67 \times 10^{-2}) = 39$.

Near the lip of the tube, a suction tends to draw down the boundary layer inside the tube and causes the sonic line to "dive" toward and intersect the lip. This continuum-to-rarefied gasdynamics phenomenon has been studied by Bird[12] using Monte Carlo techniques. While a similar trend is evident

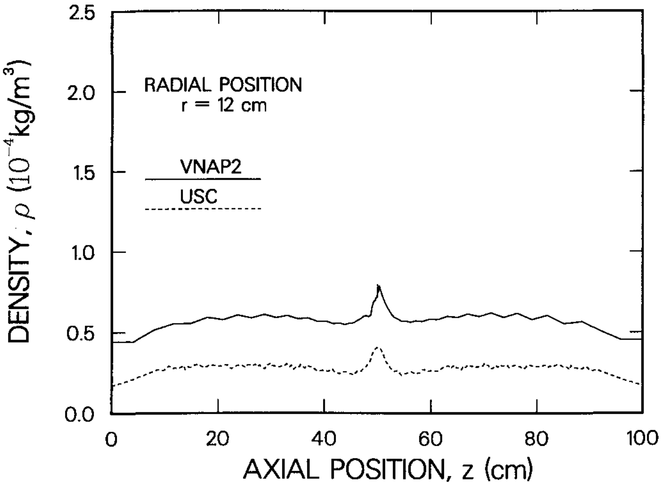

Fig. 18 Comparison of VNAP2 prediction to USC axial density data for $r = 12$ cm.

Table 3 Comparison of VNAP2 predicted to measured pressures

Point	Location	z cm	r cm	VNAP2, Pa	Experiment, Pa	Percent difference
1	Wall	99.238	15	1.04	0.711	46
2	Wall	86.284	15	2.22	1.56	42
3	Wall	77.140	15	2.53	1.51	68
4	Wall	67.996	15	2.41	1.60	51
5	Wall	58.852	15	2.12	1.33	59
6	End	100.000	0	1.04	1.04	0
7	End	109.450	0	N/A	0.689	N/A

in Fig. 10, the code may not be properly modeling conditions on the end of the tube, especially near the tube lip. The VNAP2 boundary condition used on the ends of the tube was uniform at the measured centerline value of $p_e = 1.04$ Pa (see Table 3). However, Table 3 shows that near the lip (point 1) the pressure is reduced to 0.711 Pa. This lower pressure can be transmitted upstream in the subsonic boundary layer, thereby reducing the boundary-layer thickness and further expanding the supersonic core flow. This may explain the gradually increasing density differences observed in Figs. 14-16. While these density differences are not very large locally, the target thickness that is a global integrated quantity shows a much larger discrepancy in Fig. 13.

A second possible significant source of differences may be the use of a continuum slot in the VNAP2 flow model (operating at a much lower stagnation pressure and, therefore, producing weaker shocks) as opposed to the 40 discrete (higher-pressure) holes used in the experimental model. Several other possible sources of error are believed to be of lesser importance. These include the 7.5% lower mass-flow rate in the experimental model, 5% experimental error, and the lower resolutioin of the computational grid near the ends of the tube.

Conclusions

Two-dimensional numerical solutions to the full Navier-Stokes equations representing a gas neutralizer internal flowfield have been presented for argon. These solutions were compared to three-dimensional experimental results obtained using a ⅓-scale model and the electron-beam fluorescence technique. Calculated values of the neutralizer target thickness parameter varied from 15% to two times larger than the measured values. However, the results show that general flow features, such as fairly uniform target thickness to the midradius, shock location, and axial and radial density profile shapes, were well predicted by the code before the experimental results were available. Additional calculations, using the measured tube exit-plane pressure profile together with a refined computational grid, and additional experiments using a continuum slot for gas injection are suggested by the results as ways to improve the comparison. In general, while the comparison was not completely satisfactory in all respects, the results show that VNAP2 is useful for future qualitative gas neutralizer design calculations and the evaluation of new design concepts that admit less gas into the beamline.

Acknowledgments

This work was performed under the auspices of the Department of Energy and supported by the U.S. Army Strategic Defense Command. The authors wish to thank Ms. P. Goldman, Mr. W. Hite, Ms. G. Lazarus, Mr. L. Stapf, and Ms. S. Sullivan of Los Alamos, and Mr. T. DeWitt and Mr. M. Trojanowski of USC for their assistance.

References

[1] Jansen, J., "GTA Baseline Design Report," Los Alamos National Lab, Los Alamos, NM, Rept. LA-UR-86-2775, Aug. 1986.

[2] Strickland, B. R. and Maise, G., "Joint U.S. Army BMDATC/BNL Neutralizer Workshop," Brookhaven National Lab, Upton, NY, June 1985.

[3] Strickland, B. R. and Maise, G., "Summary, 2nd Joint U.S. Army SDC/BNL Neutralizer Workshop," Brookhaven National Lab, Upton, NY, June 1986.

[4] Brook, J. W., Calia, V. S., and Muntz, E. P., "Gas Dynamic Properties of a Ring Nozzle Neutralizer," Grumman Corporate Research Center, Bethpage, NY, Rept. RE-718, July 1986.

[5] Hayward, T. D. et al., "Negative Ion Beam Processes," Los Alamos National Lab, Los Alamos, NM, Rept. LA-6019, Jan. 1976.

[6] Fuehrer, R. G., private communication, Los Alamos, NM, May 1986.

[7] Cline, M. C., "VNAP2: A Computer Program for Computation of Two-Dimensional, Time-Dependent, Compressible, Turbulent Flow," Los Alamos National Lab, Los Alamos, NM, Rept. LA-8872, Aug. 1981.

[8] MacCormack, R. W., "The Effect of Viscosity in Hypervelocity Impact Cratering," AIAA Paper 69-354, April 1969.

[9] Wegener, P. P., ed., *Molecular Beams and Low Density Gasdynamics,* Marcel Dekker, New York, 1974, pp. 188-192.

[10] Muntz, E. P., "The Electron Beam Fluorescence Technique," AGARDograph 132, Dec. 1968.

[11] Ashkenas, H. and Sherman, F. S., "The Structure and Utilization of Supersonic Free Jets in Low Density Wind Tunnels," *Rarefied Gas Dynamics,* Vol. II, edited by J. H. deLeeuw, Academic Press, New York, 1966, pp. 84-105.

[12] Bird, G. A., "Breakdown of Continuum Flow in Freejets and Rocket Plumes," *Rarefied Gas Dynamics,* Part II, edited by Sam S. Fisher, AIAA, New York, 1981, pp. 681-694.